J|A|C|S
ARTICLES

Published on Web 05/29/2009

Ordered Rock-Salt Related Nanoclusters in $CaMnO_2$

Aurea Varela,[†] Susana de Dios,[†] Marina Parras,[†] María Hernando,[†] M. Teresa Fernández-Díaz,[‡] Angel R. Landa-Cánovas,[§] and José M. González-Calbet*[,†]

Departamento de Química Inorgánica, Facultad de Químicas, Universidad Complutense de Madrid, E-28040-Madrid, Spain, Institut Laue Langevin, BP 156X, F-38042 Grenoble, France, and Instituto de Ciencia de Materiales de Madrid, CSIC, Cantoblanco, E-28049 Madrid, Spain

Received March 13, 2009; E-mail: jgalbet@quim.ucm.es

Abstract: Oxygen engineering techniques performed under adequate controlled atmosphere show that the $CaMnO_3-CaMnO_2$ topotactic reduction−oxidation process proceeds via oxygen diffusion while the cationic sublattice remains almost unaltered. Extra superlattice reflections in selected area electron diffraction patterns indicate doubling of the $CaMnO_2$ rock-salt cell along the cubic directions of a distorted rhombohedral cell originated by ordering of Ca^{2+} and Mn^{2+} ions distributed in nanoclusters into a NaCl-type matrix, as evidenced by dark field electron microscope images. The local nature of the information provided by the transmission electron microscopy techniques used to characterize the rock-salt type $Ca_{1-x}Mn_xO_2$ solid solution clearly hints at the existence of subtle extra ordering in other upper oxides of the Ca−Mn−O system. The combination of local characterization techniques like electron microscopy with more average ones like powder X-ray and neutron diffraction allows a very complete characterization of the system.

I. Introduction

Inorganic oxides, the basis of functional materials, can present two crucial features: anionic deficiency and cations able to adopt mixed oxidation states. By varying either or both of these characteristics the physicochemical properties can be tuned, giving the possibility of fabricating smart devices. Oxygen engineering, a term coined by M. Karppinen and H. Yamauchi[1] to describe techniques for both controlling and determining the precise oxygen content, is a tool for on-demand tailoring of functional oxides into new superstructures and optimized performances. Investigations of tunability of oxygen deficiency and/or oxidation states of transition metals have been reported in perovskite-related materials. Most of these studies deal with the manipulation of the anionic sublattice under reduction atmospheres and soft enough reaction conditions to allow the generation of new metastable phases which conserve the original bi- or tri-dimensional lattice matrix. These types of reactions are highly topotactic since both, reactivity and nature of final reduction product, are determined by the crystal structure of the starting material. This experimental condition, mild temperatures of reduction process, provides sufficient thermal energy to favor the oxygen ions diffusion into a cationic subcell that remains practically unalterable, leading to the stabilization of low oxidation states and unusual oxygen polyhedra of metal cations.

Mild temperatures and different reducing agents, either gases (H_2, H_2/H_2O, CO/CO_2) or metals (Zr, Ti, etc.), have been used to prepare a large number of metastable reduced phases with perovskite-type structure.[2−4] This is the case of the Sr−Fe−O system where, for many years, the brownmillerite $Sr_2Fe_2O_5$ was the most reduced phase.[5] However, by using calcium hydride at low temperatures as a reductant,[6,7] a stable $SrFeO_2$ phase with Fe^{2+} in an unexpected square planar oxygen coordination has been recently stabilized by Tsuyimoto et al.[8] More recently, a new reduced 4H-$BaSrMnO_{2+\delta}$ with Mn^{2+} in tetrahedral coordination has been isolated from the reduction process of 4H-$BaSrMnO_3$ with lithium hydride.[9] These examples show that by using binary metal hydrides as reducing agents, the reduction process takes place at remarkably low temperatures (280−300 °C) and metastable phases can be obtained. However, they can lead, under some circumstances, either to contamination with undesired cations or the incorporation of hydrogen in the structure as happens when reducing $LaSrCoO_4$ with a hydride.[7]

The system $CaMnO_{3-\delta}$ constitutes a good example of stabilization of several metastable perovskite-related phases with Mn in different oxidation states (from Mn^{4+} to Mn^{2+}). When heated

[†] Universidad Complutense de Madrid.
[‡] Institut Laue Langevin.
[§] Instituto de Ciencia de Materiales de Madrid.

(1) Karppinen M., Yamauchi H. *International Book Series: Studies of High Temperature Superconductors*; Narkilar, A. V., Ed.; Nova Science Publishers: New York, 2001; Vol. 37, p 109.
(2) Poeppelmeier, K.R.; Leonowicz, M.E.; Scanlon, J.C.; Longo, J.M.; Yelon, W.B. *J. Solid State Chem.* **1982**, *45*, 71–79.
(3) Gonzalez-Calbet, J.M.; Herrero, E.; Rangavittal, N.; Alonso, J.M.; Martinez, J.L.; Vallet-Regí, M. *J. Solid State Chem.* **1999**, *148*, 158.
(4) Hansteen, O.H.; Breard, Y.; Fjellvag, H.; Hauback, B.C. *Solid State Sci.* **2004**, *6*, 279.
(5) Shin, S.; Yonemura, M.; Ikawa, H. *Mater. Res. Bull.* **1978**, *13*, 1017.
(6) (a) Hayward, M. A.; Green, M. A.; Rosseinsky, M. J.; Sloan, J. *J. Am. Chem. Soc.* **1999**, *121*, 8843. (b) Blundred, G. D.; Bridges, A. B.; Rosseinsky, M. J. *Angew. Chem.* **2004**, *116*, 3646.
(7) Hayward, M. A.; Cussen, E. J.; Claridge, J. B.; Bieringer, M.; Rosseinsky, M. J.; Kiely, C. J.; Blundell, S. J.; Marshall, I. M.; Pratt, F. L. *Science* **2002**, *295*, 1882.
(8) Tsujimoto, Y.; Tassel, C.; Hayashi, N.; Watanabe, T.; Kageyama, H.; Yoshimura, K.; Takano, M.; Ceretti, M.; Ritter, C.; Paulus, W. *Nature* **2007**, *450*, 1062.
(9) Adkin, J.J.; Hayward, M. A. *Inorg. Chem.* **2008**, *47* (23), 10959.

 10.1021/ja901963m CCC: $40.75

under reducing atmosphere,[10] $CaMn^{4+}O_3$ is topotactically reduced to $CaMn^{3+}O_{2.5}$ through intermediate oxygen-deficient perovskite phases with ordered oxygen vacancies.[2,11] In this compositional range, the cationic structural framework of the oxidized precursor $CaMnO_3$ is preserved. The final product of the $CaMnO_3$ reduction process is $CaMn^{2+}O_2$, a rock-salt-related phase. These ABO_3-$A_2B_2O_5$ transformations proceed through the elimination of some oxygen atoms keeping unalterable the remaining anionic sublattice. However, the structural differences between the perovskite- and the rock-salt-related phases suggest a strong diffusion of oxygen atoms when reducing $Ca_2Mn_2O_5$, where all Mn^{3+} is square pyramidal coordinated,[12,13] to $CaMnO_2$ where all Mn^{2+} is octahedrally coordinated.[14] Although the XRD study of the reversible reduction process has been reported,[10] the topotactic structural relationship between oxidized precursor and the reduced product have not been yet elucidated. Since these processes are fully reversible it could be inferred that the cationic sublattice in the final reduction product, $CaMnO_2$, should remain almost unalterable, leading to some cationic ordering.

$CaMnO_2$, the $x = 0.5$ composition of the well-known $Ca_{1-x}Mn_xO$ solid solution, presents a rock-salt-type structure. This solid solution can be formed along the whole range of composition in spite of the large disparity in size (≈20%) between the ionic radii of Mn^{2+} and Ca^{2+} ions in octahedral coordination. Actually, XRD study shows that Ca^{2+} and Mn^{2+} are randomly distributed over all cationic sites of the NaCl-type structure leading to a true substitutional solid solution.[14−16] However, a deviation from the ideality respect of the volume change of the unit cell is observed for the solution of CaO in MnO.[17] This feature could reflect the presence of some type of cationic order undetected by conventional structural techniques such as X-ray or neutron diffraction. In spite of this observation, no detailed microstructural study has been performed in this system which, up to now, remains like a real solid solution.

Herein we report the study of the reduction-oxidation process: $CaMnO_3$ (perovskite-type) ↔ $CaMnO_2$ (NaCl-type). This paper describes the synthesis, the structural and microstructural study, by X-ray, neutron diffraction, high resolution electron microscopy (HREM), and associated techniques, and the magnetic susceptibility of $CaMnO_2$ (prepared via topotactic reduction and solid state reaction). For the first time, this work shows that Ca and Mn cations are not randomly distributed over the available metal positions in the NaCl structure, but short ordered domains are present. The topotactic structural relationship between $CaMnO_3$ and the fully reduced $CaMnO_2$ is established.

II. Experimental Section

Sample Preparation. Black polycrystalline starting material $CaMnO_{3-\delta}$ was prepared by thermal decomposition of the solid solution $CaMn(CO_3)_2$. This precursor was precipitated from an aqueous acid solution containing $CaCO_3$ (Aldrich, 99%) and $MnCO_3$ (Aldrich, 99,9%) in a 1:1 ratio by adding a large excess of ammonium carbonate (Panreac 98%). The precipitate was dried and then heated in an alumina crucible at 950 °C in air for 24 h. Then, the sample was treated at 1100 °C for two days and finally quenched to room temperature. This process was repeated with intermediate grinding in order to ensure homogeneity.

Light green polycrystalline $CaMnO_2$ samples have been prepared by two methods:

***R*-$CaMnO_2$: from the Reduction Process of $CaMnO_{3-\delta}$.** The reduction was performed in a CAHN D-200 electrobalance by heating the starting material at 6°C/min up to 665 °C under 0.3 bar H_2/0.2 bar He atmosphere. The annealing temperature is kept constant for some hours in order to ensure constant weight. The final product of the reduction process corresponds to a crystalline single phase with the composition $CaMnO_2$.

***S*-$CaMnO_2$: Solid-State Reaction from CaO (Aldrich, 99%) and MnO (Aldrich, 99%) in a 1:1 Ratio Heated at 1000 °C in Flowing 5% H_2/95% Ar Atmosphere.** This process was repeated several times with intermediate grinding in order to ensure homogeneity.

Characterization. The average cationic composition of the samples was determined by microprobe analysis in a JSEM-8600 scanning electron microscope working at an acceleration voltage of 10 KV. In addition, the local composition was analysed by energy-dispersive X-ray spectroscopy (EDS) with an INCA analyser system attached to a JEOL 2000 FEG electron microscope.

The overall oxygen content was determined by thermogravimetric analysis using a CAHN D-200 electrobalance, which allows the determination of variations of the oxygen content within $\pm 1 \times 10^{-3}$ on a sample of about 100 mg working under 0.5 bar gas atmosphere. Experiments were performed by reduction under a 0.3 bar H_2/0.2 bar He atmosphere with a heating rate of 6 °C/min up to a maximum temperature of 665 °C. The reoxidation process of the $CaMnO_2$ samples was carried out under oxygen atmosphere (1 bar), heating the specimen up to 550 °C at a rate of 4 °C/min. The oxygen content was determined from the weight difference between starting and final products.

Powder X-ray diffraction (XRD) patterns were collected using CuK_α radiation ($\lambda = 1.5418$ Å) at room temperature on a PHILIPS X′PERT diffractometer equipped with a graphite monochromator. Neutron powder diffraction (NPD) data were collected at room temperature and at 5 K on the high-resolution powder diffractometer D2B (S-$CaMnO_2$) and D1A (R-$CaMnO_2$) at the Institute Laue Langevin (ILL), Grenoble (France). D2B diffractometer works with neutrons of wavelength 1.594 Å and the angular range covered by the detector expands from 0° to 160° in scattering angle (step size 0.05°). The two-axis powder diffractometer D1A works with neutrons of wavelength 1.908 Å and the angular range covered by the detectors expands from −10° to 160° with a step size of 0.05°. Diffraction data were analysed by the Rietveld method[18] using the Fullprof program.[19]

The morphological study was carried out with a JSM-6330F FEG scanning electron microscope working at 20 kV. Selected area electron diffraction (SAED) and HREM were performed in a JEOL 2000 FX electron microscope (double-tilt specimen holder: ±45°) and JEOL 3000 FEG electron microscope, fitted with a double tilting goniometer stage (±20°). Electron energy loss spectroscopy (EELS) data and dark field images were obtained from a Philips CM200 FEG electron microscope (fitted with a XEDS analyzer EDAX DX4). EELS experiments were carried out with a Gatan Image Filter GIF 200 with ∼0.9 eV energy resolution. EELS spectra of the Mn L_3L_2 white lines and of the O K-edge were acquired in diffraction mode with a collection angel of $\beta \approx 11$ mrad. The L_3/L_2 intensity ratio was measured after the subtraction of the background modeled according to Pearson method.[20]

(10) Reller, A.; Davoodabady, G.; Oswald, H. R. *Thermochim. Acta* **1985**, *83*, 121.
(11) Reller, A.; Thomas, J. M.; Jefferson, D. A.; Uppal, M. K. *Proc. R. Soc. London A* **1984**, *394*, 223.
(12) Poeppelmeier, K. R.; Leonowicz, M. E. J. C.; Longo, J. M. *J. Solid State Chem.* **1982**, *44*, 89.
(13) Caignaert, V.; Hervieu, M.; Hguyen, N.; Raveau, B. *J. Solid State Chem.* **1986**, *62*, 281.
(14) Natta, G.; Passerini, L. *Gazz. Chim. Ital.* **1929**, *59*, 129.
(15) Jay, A.H.; Andrews, K.R. *Nature* **1944**, *154*, 116.
(16) Fubini, B.; Stone, F.S. *J. Chem. Faraday Trans. I* **1983**, *79*, 1215.
(17) Otero Arean, C.; Stone, F.S. *J. Chem. Faraday Trans. I* **1979**, *75*, 2285.
(18) Rietveld, H. M. *J. Appl. B Crystallogr.* **1969**, *2*, 65.
(19) Rodríguez-Carvajal, J. *Physica B* **1993**, *192*, 55.
(20) Pearson, D.H.; Ahn, C.C.; Fultz, B. *Phys. Rev. B* **1993**, *47*, 8471.

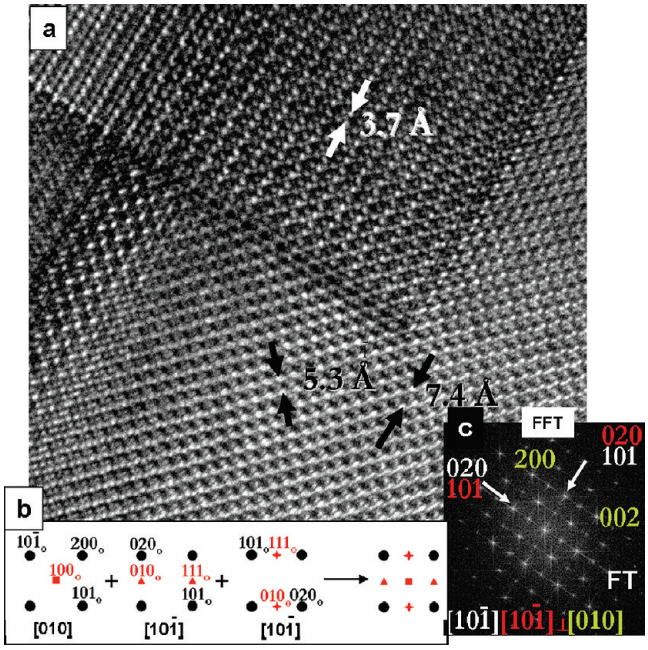

Figure 1. (a) HREM image corresponding to the starting material $CaMnO_{2.96}$ along the $[001]_c$ zone axis. (b) Schematic representation of the patterns corresponding to the three perpendicular domains. (c) Corresponding FFT.

DC magnetization was measured by a commercial superconducting quantum interface device (SQUID) magnetometer from Quantum Design. Magnetotransport measurements were performed under magnetic fields up to 50 kOe in the range ~1.8−400 K.

III. Results and Discussion

The XRD pattern of the $CaMnO_{2.96}$ starting material can be indexed on the basis of an orthorhombic unit cell (Pnma) perovskite-type[2] with lattice parameters, $a = 5.281(2)$ Å, $b = 7.456(3)$ Å, and $c = 5.266(2)$ Å. No impurity phases were detected.

SAED and HREM characterization of $CaMnO_{2.96}$ shows a microdomain microstructure as a consequence of multitwinning previously described in slightly distorted orthorhombic ABO_3 perovskites.[21] Actually, Figure 1a shows the HREM corresponding to $CaMnO_{2.96}$ along $[001]_c$. This image shows different domains that are a consequence of the juxtaposition of three identical reciprocal cells with parameters $a = \sqrt{2}a_c$, $b = 2a_c$ and $c = \sqrt{2}a_c$ (schematically represented in Figure 1b), with the *b*-axis randomly distributed in the three space directions, as reflected in Figure 1c.

R-$CaMnO_2$ was obtained from the reduction of the starting material $CaMnO_{2.96}$.Thermogravimetric reduction curve shows an abrupt weight loss at relatively low temperature (400 °C) followed by a plateau. The green final product was identified by XRD as $CaMnO_2$ (*R*-sample). From the experimental 11% weight loss, the anionic composition of the starting material results to be $CaMnO_{2.96}$.

As mentioned in the Experimental Section, *S*-$CaMnO_2$ has been also prepared by solid-state reaction. The XRD patterns of both samples, *R* and *S,* can be indexed on the basis of a cubic ($Fm\bar{3}m$) single-phase rock-salt-type, no evidence for additional maxima being found. The patterns have been refined by the Rietveld method by using the rock-salt data. The refined unit cell parameters for both *R* and *S* samples correspond to $a = 4.629(2)$ and $4.620(7)$ Å, respectively.

For further insight into the structural features of the samples, neutron powder diffraction (NPD) study was performed. Figure 2 shows the graphic results of the fitting of the NPD pattern, taken at 293 K, and the difference between observed and calculated data corresponding to *R* (Figure 2a) and *S* (Figure 2b) samples. The refined parameters are gathered in Table 1.

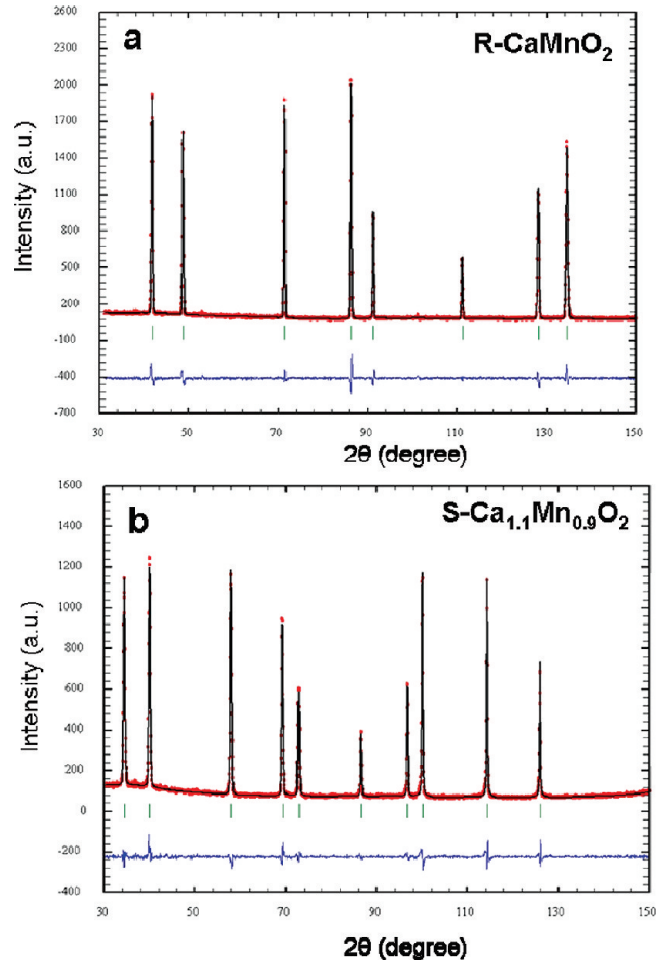

Figure 2. Rietveld refinement of neutron diffraction data at room temperature corresponding to (a) *R*-$CaMnO_2$ (wavelength of neutrons 1.908 Å) and (b) *S*-$Ca_{1.1}Mn_{0.9}O_2$ (wavelength of neutrons 1.594 Å). The solid lines and overlying dots indicate the calculated and observed intensities. The difference between the observed and calculated profiles is plotted at the botton in blue.

Table 1. Structural Parameters Obtained from the Refinement of NPD Data at 300 K of *S*- and *R*-$CaMnO_2$ Samples

	R-$CaMnO_2$	*S*-$Ca_{1.1}Mn_{0.9}O_2$
a (Å)	4.63135(2)	4.67710(4)
Ca/Mn (1/2, 1/2, 1/2)		
Occ	0.502(1)/0.497(1)	0.549(2)/0.451(2)
B (Å^2)	0.35(2)/0.35(2)	0.49(11)/0.49(11)
O (0, 0,0)		
Occ	1.0	1.0
B (Å^2)	0.78(3)	1.113(19)
R_B	1.57	1.87
R_{wp}	6.27	6.29
R_{exp}	4.35	3.42
χ^2	2.07	3.38

(21) (a) White, T.J.; Segall, R.L.; Barry, J.C.; Hutchison, J.L. *Acta Crystallogr.* **1985**, *B41*, 93. (b) Vegas, A.; Vallet-Regí, M.; González-Calbet, J.M.; Alario-Franco, M.A. *Acta Crystallogr.* **1986**, *B42*, 167.

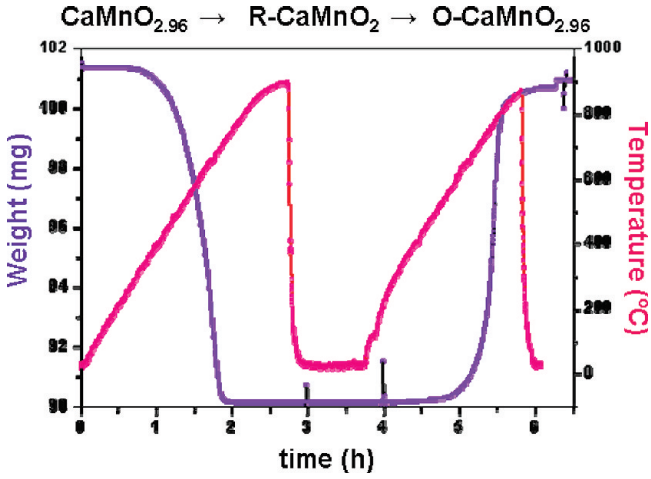

Figure 3. Thermogravimetric curves corresponding to the reduction/reoxidation processes: $CaMnO_{2.96} \rightarrow$ *R*-$CaMnO_{2.0} \rightarrow$ O-$CaMnO_{2.96}$.

These results agree with the XRD ones. No extra maxima which could be associated to any kind of cationic order are visible, suggesting a random distribution of Mn and Ca atoms over the available crystallographic positions (Table 1). The refinement of the metal occupancy factors, see Table 1, shows that *R*-$CaMnO_2$ maintains the Ca/Mn = 1:1 nominal ratio of the oxidized sample. On the contrary, a slight deviation from the nominal cationic composition, $CaMnO_2$, is observed in the prepared sample where a Ca/Mn= 1.1:0.9 ratio, i.e., $Ca_{1.1}Mn_{0.9}O_2$ is obtained.

Reversibililty of the Reduction ⇔ Oxidation Process: $CaMnO_3$ ⇔ $CaMnO_2$. The thermal stability of the samples was investigated by using thermogravimetric analysis. Reoxidation process of *R*-$CaMnO_2$ was performed in the electrobalance heating up to 665 °C, under 1 bar O_2. The thermogravimetric curves of reduction/reoxidation processes are depicted in Figure 3. $CaMnO_2$ reoxidizes at moderate temperature leading to the starting $CaMnO_{2.96}$ (labelled as O-$CaMnO_{2.96}$ phase). Therefore, the $CaMnO_{2.96} \Leftrightarrow CaMnO_2$ reaction is reversible and both reduction and reoxidation processes occur with a rapid kinetics. On the other hand, under the above experimental conditions, the oxidation of *S*-$Ca_{1.1}Mn_{0.9}O_2$, gives rise to O-$Ca_{1.1}Mn_{0.9}O_{2.96}$ perovskite-type as final oxidation product. XRD patterns of both oxidized samples are similar to that of the starting material, $CaMnO_{2.96}$.

Figure 4a−d is a set of SEM micrographs showing the morphological changes associated to the reduction-reoxidation processes of the $CaMnO_{2.96}$ starting material. As expected, $CaMnO_{2.96}$ particles exhibit a sintered microstructure with rounded particles and quite a certain degree of sintering (Figure 4a). The average size varies between 1 and 3 μm. Figure 4b shows the SEM micrograph corresponding to *R*-$CaMnO_2$. As can be seen, the morphology of the starting sample drastically changes when heating under H_2 atmosphere leading to hexagonally faceted platelet-like aggregates. This morphology is kept when $CaMnO_2$ is reoxidized to O-$CaMnO_{2.96}$ (Figure 4c); note that each grain is formed by very small crystallites. *S*-$Ca_{1.1}Mn_{0.9}O_2$ sample is formed by spherical cubic multishape-like particles of 1−4 μm (Figure 4d). This morphology is maintained in O-$Ca_{1.1}Mn_{0.9}O_{2.96}$ as evidenced in Figure 4e where the presence of small crystallites is also appreciated.

The microstructural characterization of the reoxidized samples shows a similar microdomain microstructure to that of starting $CaMnO_{2.96}$, although both domain size and orthorhombic structural distortion are smaller leading to multitwinned crystals, as observed in the image of Figure 1a.

Microstructural Study of $CaMnO_2$ Rock-Salt-Type Samples. The particular features of the reversible reduction-oxidation process of $CaMnO_{2.96}$ (low temperature and rapid kinetics) point up to a topotactic oxidation-reduction mechanism. In this sense, the presence of cationic Ca/Mn order could be expected. Since neither XRD nor NPD detect cationic ordering through the different crystalline domains, we have performed a study by SAED and HREM in order to get structural information at the local level.

SAED study of both *R*-$CaMnO_2$ and *S*-$Ca_{1.1}Mn_{0.9}O_2$ samples shows the same structural features regardless of the synthesis pathway and the cationic ratio. Figure 5a corresponds to the SAED pattern of *R*-$CaMnO_2$ along the [001] zone axis where all reflections can be indexed on the basis of a cubic $Fm\bar{3}m$ cell characteristic of the rock-salt structural type. The HREM (Figure 5b) shows a fully ordered material with interplanar distances of 2.3 Å, corresponding to d_{200} and d_{020}. However, a careful examination of the contrast variation of this image evidences (see enlargement), in some small areas of the crystal, bright spots of different intensity that could be associated to some kind of cationic order. In fact, the presence of ordering is reflected in the SAED pattern along the [$1\bar{1}\bar{2}$] zone axis (Figure 6a). Actually, besides the basic spots corresponding to the cubic

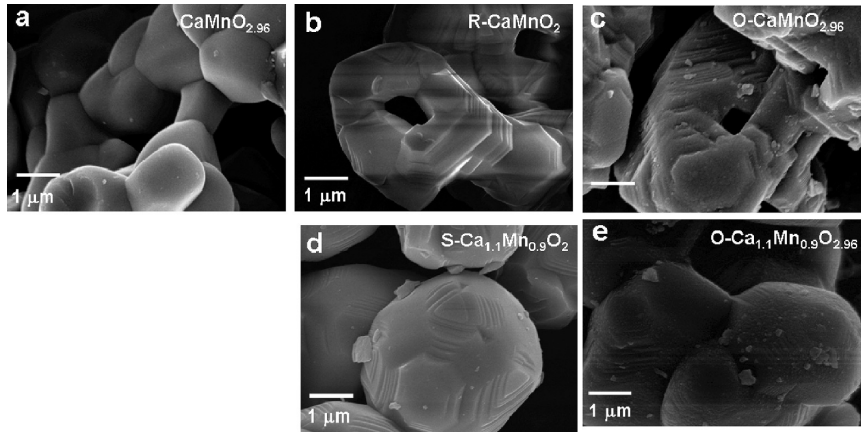

Figure 4. SEM micrographs corresponding to the reduction-reoxidation processes: (a) $CaMnO_{2.96} \rightarrow$ (b) *R*-$CaMnO_2 \rightarrow$ (c) O-$CaMnO_{2.96}$. SEM micrographs for (d) *S*-$Ca_{1.1}Mn_{0.9}O_2$ and (e) oxidized final product O-$Ca_{1.1}Mn_{0.9}O_{2.96}$.

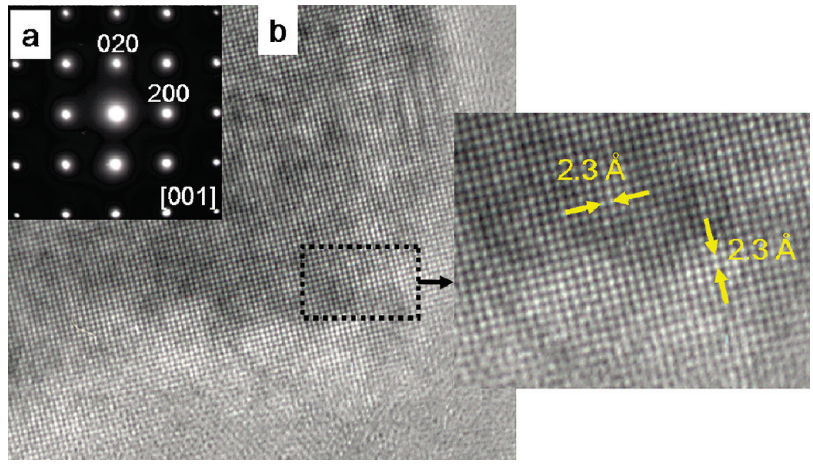

Figure 5. (a) SAED pattern corresponding to *R*-$CaMnO_2$ along the [001] zone axis. (b) Corresponding HREM image.

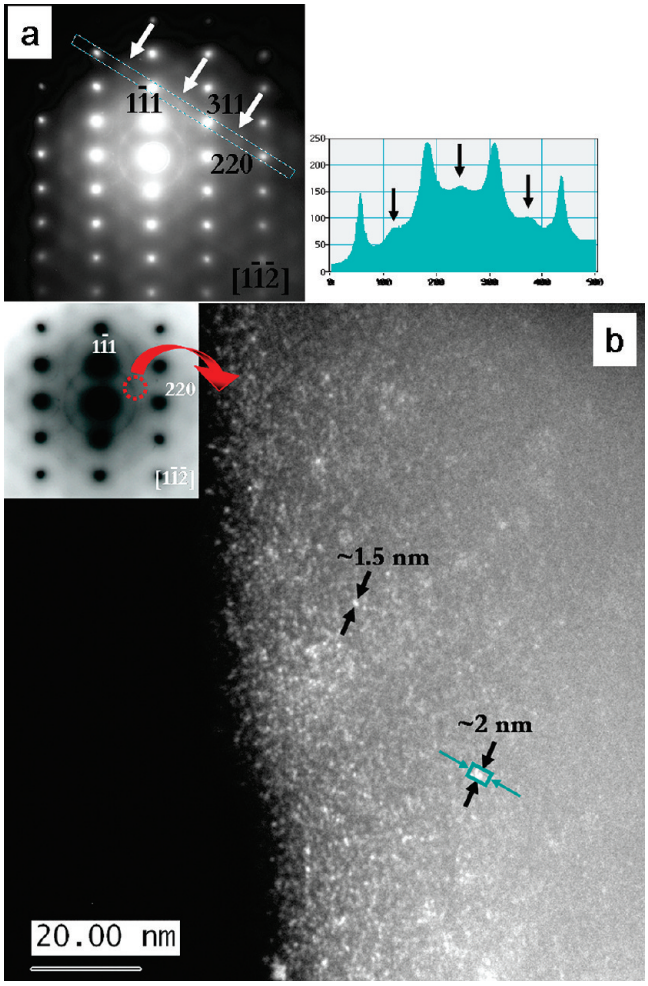

Figure 6. (a) SAED pattern corresponding to *S*-$CaMnO_2$ along the $[1\bar{1}\bar{2}]$ zone axis. (b) Dark-field image taken with the weak spot doubling the $(311)^*_{NaCl}$ (indicated by an arrow in the pattern).

NaCl-type phase, weak diffuse extra reflections are seen at 1/2 (311)*. This feature appears in all the observed crystals. These extra superlattice reflections indicate doubling of the rock-salt cell along the cubic {111} directions giving rise to a distorted rhombohedral unit cell of parameter $a_R = \sqrt{2}a_{NaCl}$.

These diffuse blocks suggest the presence of short range order (SRO) which could be distributed along the crystal as small clusters dispersed inside the basic rock-salt matrix. In order to reveal the size and distribution of the areas exhibiting SRO, dark-field (DF) imaging was carried out. A small objective aperture was placed on the diffuse reflection at 1/2 (311)* to form the image. In this way only the regions which contain the satellite reflection at 1/2 (311)* will light up. Due to the weak intensity of this reflection, the zone axis orientation was slightly tilted away from perfect orientation in such a way that the 1/2 (311)* reflection was strongly excited.[22] In these conditions, good quality DF images could be obtained showing two kinds of areas with different contrast (Figure 6b). Bright zones, of around 1−3 nm in length, correspond to domains with extra order of the NaCl-type. This short-range order must be originated by a particular Ca/Mn arrangement at microscopic level. These areas coexist with less-bright zones corresponding to a disordered NaCl-type matrix. Therefore, the dark field image evidences that the microstructure of the reduced $CaMnO_2$ crystals are constituted by ordered nanoclusters into a NaCl-type matrix. The weakness of the extra observed reflections in the SAED pattern reflects probably the small size and the variability in the extension of the short-ordered domains in the crystals. Such rhombohedral distortion can take place along all the equivalent cubic (111) directions generating different crystallographic domains and giving rise to a nanotwinned crystal with an average cubic symmetry.

It is worth recalling that the presence of order in the Ca−Mn−O system is usually attributed to Mn in several oxidation states and different coordination. In our case, thermogravimetric analysis of both *R* and *S* samples indicates that all Mn is present as Mn^{2+}. However, to ensure these results and accurately determine the Mn oxidation state, the reduced samples were characterized by EELS spectroscopy. For this purpose, MnO was also analyzed to provide EELS valence standard to compare with EELS spectra of *R*-$CaMnO_2$ and *S*-$Ca_{1.1}Mn_{0.9}O_2$ compounds. As is well known, Mn_2O_3 is also present in commercially available MnO; thus, to obtain pure single phase $Mn^{2+}O$, commercial MnO was reduced under H_2 atmosphere.

EELS spectra corresponding to both *S* and *R* samples are similar and show the same ELNES features. Figure 7a shows the EELS spectra corresponding to *R*-$CaMnO_2$ sample where Ca−$L_{2,3}$, Mn−$L_{2,3}$ and O−K ELNES are observed. EELS measurements (background subtracted from the experimental spectra) of Mn−$L_{2,3}$ and O−K edge for *R*-$CaMnO_2$ and MnO are shown in Figure 7b−c and Figure 7d−e, respectively. The shape of Mn−$L_{2,3}$ edge, characteristic of Mn^{2+} in octahedral

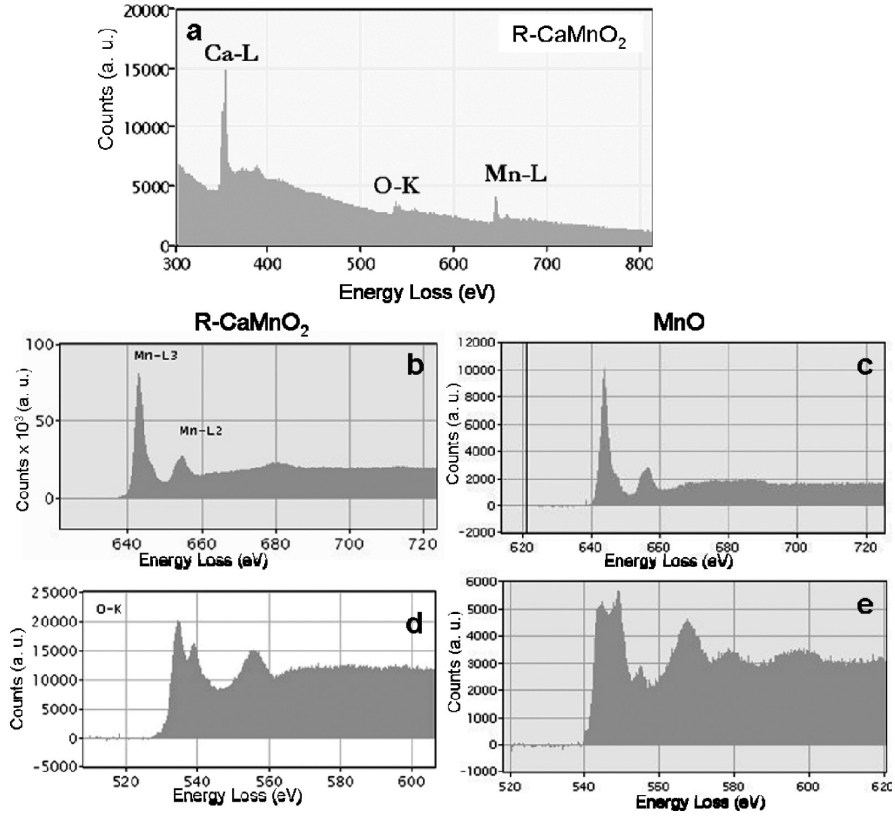

Figure 7. (a) EELS spectra corresponding to *R*-$CaMnO_2$, showing the Ca−$L_{2,3}$, Mn−$L_{2,3}$ and O−K edges. EELS spectra (background subtracted) showing Mn−$L_{2,3}$ (b and c) and O−K edges (d and e) taken from *R*-$CaMn^{+2}O_2$ and $Mn^{2+}O$ reference sample, respectively.

Table 2. Mn−$L_{2,3}$ ELNES Data from *R,S*-$CaMnO_2$ and MnO (Reference Sample and Published by Schmid et al.[26])

sample	*S*-$Ca_{1.1}Mn_{0.9}O_2$	*R*-$CaMnO_2$	MnO	MnO[26]	$MnCO_3$[26]
energy (eV) Mn−L_3[a]	643.8	644.5	644.5	641.2	640.8
Energy (eV) Mn−L_2[a]	655.5	656.0	656.0	652.7	652.5
$\Delta E_{Mn(L_2-L_3)}$ (eV)	11.7	11.5	11.5	11.5	11.7
intensity ratio (L_3/L_2)	4.3	4.3	4.1	3.9	4.1

[a] $L_{2,3}$ white-line peak (max) positions.

coordination, is similar for both samples, although a subtle difference is observed in the shape of the O−K edge due to the dominating O−K ELNES from the CaO matrix in $CaMnO_2$. Mn−$L_{2,3}$ and O−K ELNES data from *S* and *R* samples and MnO are gathered in Table 2. The intensity ratio Mn(L_3/L_2) and energy difference $\Delta E(L_2-L_3)$ values are in agreement with those exhibited by Mn^{2+} in octahedral oxygen coordination in MnO and $MnCO_3$.[23−26]

EELS analysis confirm that Mn is only present as divalent Mn^{2+} in both $CaMnO_2$-type samples. From this, it can be concluded that the microstructural features observed by both SAED and HREM techniques are related to an ordered arrangement of Ca and Mn over the metal sites of the rock-salt structure, at least in small regions of the crystals. As mentioned above, these ordered nanoclusters coexist with the NaCl-type matrix in $Ca^{II}Mn^{II}O_2$ samples.

The $CaMnO_3$−$CaMnO_2$ reduction process takes place at moderate temperature, 400 °C; these conditions provide sufficient thermal energy to favor oxygen diffusion allowing the rearrangement of the oxygen ions through the structure while the cationic subcell remains almost unalterable leading to a short-range cationic order situation in $CaMnO_2$. Keeping this in mind, it is worth recalling that the short range cationic order has also been observed in the sample prepared by solid state reaction at 1000 °C. The use of high temperature in preparative chemistry leads to thermodynamically stable end-product and the nature of the product does not seem to depend on the pathway followed by the reaction. According to that, it can be suggested that the cationic order is not determined by the topotactic reduction process but it is inherent to the $Ca_{1-x}Mn_xO_2$ solid solution. In spite of this, the reversibility and ease of the above mentioned reduction process indicate a topotactic relationship between both $CaMnO_3$ (perovskite-type) and $CaMnO_2$ (NaCl-type) structures.

The ordered structure of $CaMnO_2$ can be easily derived from the perovskite structure viewed along the (111) direction. Ca and Mn atoms alternate in an ordered 1:1 sequence following equivalent directions along the cubic perovskite (Figure 8a). From this cationic arrangement, an ordered rhombohedral NaCl-type superstructure is generated where Ca and Mn are distributed in alternate planes along the stacking direction of the basic cubic rock-salt structure (Figure 8b). For a better comparison between both structures it is useful to describe the perovskite structure from a rhombohedral unit cell of parameters, $a_R \approx \sqrt{3}a_P$ (Figure 9a). By considering both rhombohedral cationic subcells, the structural relationship between $CaMnO_3$ and ordered $CaMnO_2$ is easily established (Figure 9b). The unit cell parameters and the crystallographic relationships between both structures are also shown in Figure 9.

The reduction from $CaMnO_3$ to $CaMnO_2$ implies the elimination of two out of every three oxygen atoms centred at the edges and the rearrangement of the remaining one located at one vacant position (1/4, 1/4, 1/4) inside the perovskite cell. From this atomic rearrangement, in which calcium and manganese ions keep the atomic positions of the perovskite starting material,

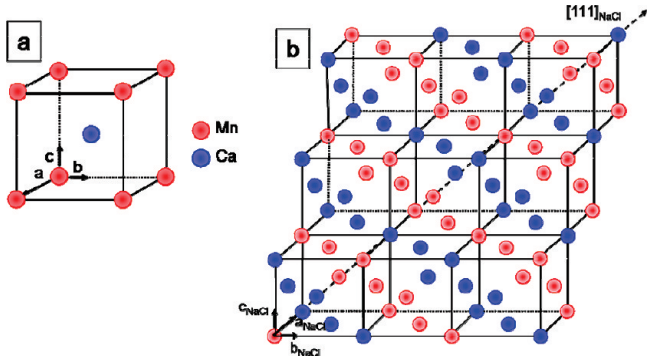

Figure 8. Schematic representation of the (a) cubic perovskite structure and (b) NaCl-type structure with ordered cationic distribution ···Ca−Mn−Ca−Mn··· along the stacking direction. Oxygen anions omitted for clarity.

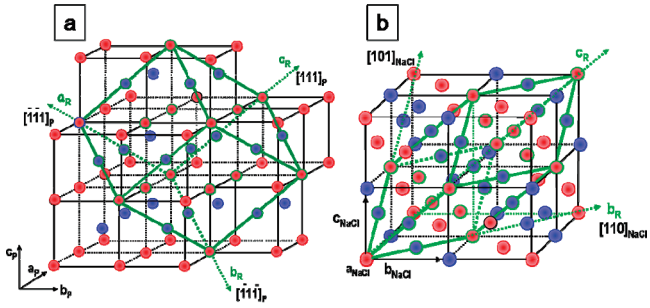

Perovskite-type	NaCl-type
$a_R \parallel [\bar{1}\bar{1}1]_P$	$a_R \parallel [101]_{NaCl}$
$b_R \parallel [\bar{1}1\bar{1}]_P$	$b_R \parallel [110]_{NaCl}$
$c_R \parallel [111]_P$	$c_R \parallel [011]_{NaCl}$
$a_R \approx (\sqrt{3})a_p^* \approx 6.58$ Å, $\alpha \approx 60°$	$a_R \approx (\sqrt{2})a_{NaCl}^{**} \approx 6.55$ Å, $\alpha \approx 60°$

Figure 9. Schematic representation of (a) cubic, a_p (black) and rhombohedral a_R (green) unit cell of perovskite structural type; (b) cubic (a_{NaCl}) rhombohedral (a_R) unit cell of the NaCl structural type. Unit cell parameters and crystallographic relationships of both rhombohedral cationic subcells ($^*a_P$ ($CaMnO_3$) ≈ 3.8 Å; $^{**}a_{NaCl} = 1/2[a_{MnO} + a_{CaO}] = 4.628$ Å).

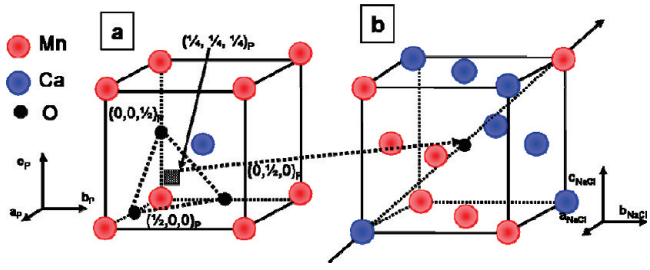

Figure 10. Elimination and rearrangement of oxygen atoms in the structural transformation $CaMnO_{2.96}$ (cubic perovskite) (a) → $CaMnO_2$ (NaCl-type) (b) via a topotactic route.

an ordered NaCl-type cell is obtained. This mechanism can be easily visualized in Figure 10 where both the perovskite and ordered NaCl-type unit cells are shown.

It is worth recalling that the same cationic ordering scheme is found in the dolomite-like compound, Kutnahorite, with $Ca_{1-x}Mn_x(CO_3)$ ($0.45 \le x \le 0.50$) composition[27] and unit cell

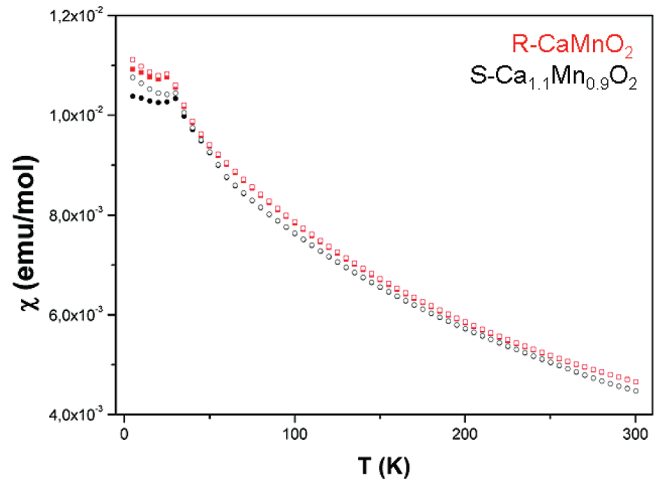

Figure 11. Temperature dependence of the magnetic susceptibility measured at 1 KOe for *R*-$CaMnO_2$ and for *S*-$Ca_{1.1}Mn_{0.9}O_2$.

parameters $a \approx a_{NaCl}\sqrt{2}/2 \approx 3.26$ and $c \approx a_{NaCl}\,2\sqrt{3} \approx 16.02$ Å. The presence of the Ca/Mn cationic order depends on the Kutnahorite specimen origin, suggesting that the ordering is associated with both, the Ca/Mn ratio and the genesis process of the specimen.[27,28]

Magnetic Properties. Magnetic susceptibility versus temperature curves for *R*-$CaMnO_2$ and *S*-$Ca_{1.1}Mn_{0.9}O_2$ measured at zero field cooling (ZFC) and under 1000 Oe field on cooling (FC) are shown in Figure 11. In the temperature range from 200 to 300 K, the magnetic susceptibility can be fitted to the Curie−Weiss law, leading to an extrapolated Curie−Weiss constant $\theta = -174.1$ and -152.4 K for *R* and *S* samples, respectively, and a paramagnetic effective moment of 5.7 μ_B/Mn cation. This result is in agreement with the calculated paramagnetic moment for Mn^{2+} in high spin electronic configuration (5.92 μ_B). At low temperatures, around 30 K, the magnetic susceptibility shows a maximum for both samples that could be associated to the antiferromagnetic onset seen in the MnO oxide.[29] A small difference between zero-field-cooled (M_{ZFC}) and field-cooled (M_{FC}) magnetizations is observed at low temperature. This irreversibility has been previously described by Kolesnik et al.[30] in the $Ca_{1-x}Mn_xO$ system for low Mn concentration ($x = 0.25-0.4$) and has been associated to spin glass behaviour characteristic of diluted magnetic systems. For a deeper insight on the magnetic structure of these samples, a neutron diffraction characterization at low temperature has been carried out. The magnetic structure was refined from the high-resolution diffraction data collected at 5 K. Besides the peaks of the nuclear structure (cubic cell, $Fm\bar{3}m$), extra reflections can be observed, corresponding to magnetic Bragg peaks. These peaks were analysed using a magnetic unit cell with double dimensions than the structural one with a propagation vector $k = (1/2\ 1/2\ 1/2)$. The calculated and experimental patterns are shown in Figure 12a and b. The results of the refinement of the best fit are summarized in Table 3. The

(22) Withers, R.L.; Otero-Diaz, L.C.; Thompson, J.G. *J. Solid State Chem.* **1994**, *111*, 283.
(23) Manson, J.L.; Leone, P.; Euzen, P.; Palvadeau, P. *Microsc. Microanal. Microstruct.* **1994**, *5*, 79.
(24) Kurata, H.; Colliex, C. *Phys. Rev. B* **1993**, *48* (4), 2102.
(25) Wang, Z.L.; Yin, J.S.; Jiang, Y.D.; Zhang, J. *Appl. Phys. Let* **1997**, *70* (25), 3362.
(26) Schimd, H.K.; Mader, W. *Micron* **2006**, *37*, 426.
(27) Goldsmith, J.R.; Graf, D.L. *Geochim. Cosmochim. Acta* **1957**, *11*, 310.
(28) Peacor, D.R.; Essene, E.J.; Gaines, A.M. *Am. Mineral.* **1987**, *72*, 319.
(29) Tyler, R.W. *Phys. Rev. B* **1933**, *44*, 776.
(30) Kolesnik, S.; Dabrowski, B. *J. Supercond. Novel Magn.* **2003**, *16* (3), 501.

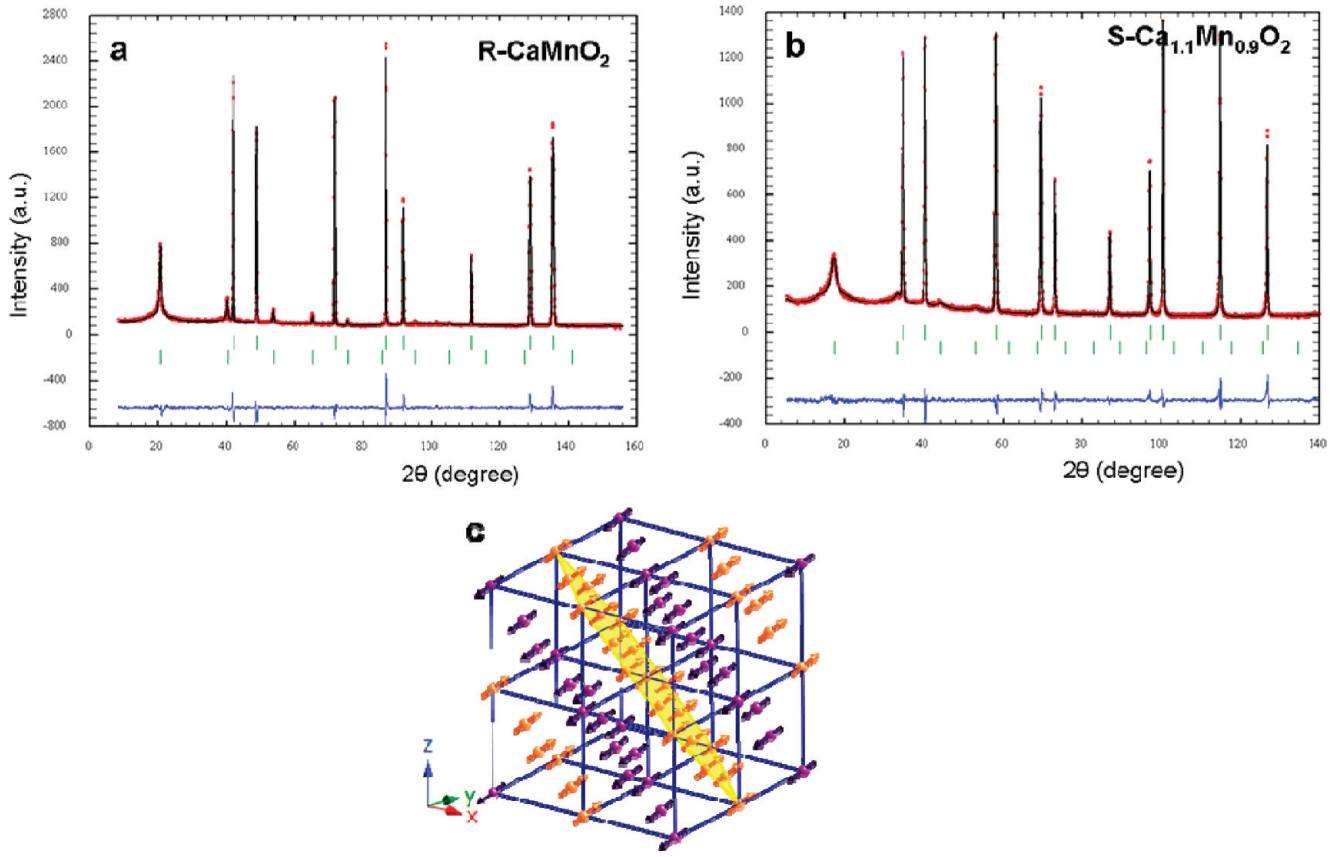

Figure 12. Magnetic characterization of $CaMnO_2$ samples. Rietveld refinement of high-resolution neutron diffraction at low temperature (5 K) for (a) *R*-$CaMnO_2$ (wavelength of neutrons 1.908 Å) and (b) *S*-$Ca_{1.1}Mn_{0.9}O_2$ (wavelength of neutrons 1.594 Å). (c) Magnetic structure with $a = 2a_{NaCl}$ magnetic unit cell. The difference between the observed and calculated profiles is plotted at the botton in blue.

Table 3. Structural Parameters Obtained from the Refinement of NPD Data at 5 K of *R*-$CaMnO_2$ and *S*-$Ca_{1.1}Mn_{0.9}O_2$

	R-$CaMnO_2$	*S*-$Ca_{1.1}Mn_{0.9}O_2$
a (Å)	4.61845(2)	4.63449(15)
Ca/Mn Occ	0.504(2)/0.496(2)	0.544(2)/0.456(2)
B (Å^2)	0.27(3)/0.27(3)	0.39(6)/0.39(6)
M (μ_B)	0/3.77(2)	0/3.82(2)
O Occ	1.0	1.0
B (Å^2)	0.717(10)	0.951(11)
R_B	3.83	1.16
R_{mag}	5.14	5.37
R_{wp}	8.23	4.95
R_{exp}	4.30	2.94
χ^2	3.67	2.83

magnetic moment obtained for both samples is close to 3.8 μ_B, in agreement to that found for Mn^{+2} in MnO.[31]

The magnetic structure is shown in Figure 12c. The antiferromagnetic order consists of (111) sheets of ferromagnetically ordered Mn^{2+} ions, which are antiferromagnetically coupled to the neighboring sheets along the (111) direction. MnO presents, below the Néel temperature (118 K), the same antiferromagnetic order. Nevertheless, it suffers a slight rhombohedral deformation from the original cubic unit cell due to a compression along the (111) direction, converting cubic angles from 90° to 90.62°.[32,33] This magnetostrictive distortion is not found in any of $CaMnO_2$ samples. The presence of diamagnetic Ca^{2+} with respect to MnO should weaken the strength of the antiferromagnetic interactions originating the lack of magnetostriction and decreasing the Néel temperature (from 118 K for MnO to 30 K for $CaMnO_2$).

The intensity of the magnetic peaks is different for both samples, higher relative intensity being observed in *R*-$Ca_{1.0}Mn_{1.0}O_2$. This fact can be attributed to the slight variation in the cationic composition: $Ca_{1.0}Mn_{1.0}O_2$ and $Ca_{1.10}Mn_{0.90}O_2$. Actually, the higher Mn concentration in the *R* sample should reinforce the magnetic interactions increasing the intensity of the magnetic peaks.

IV. Concluding Remarks

The reduction process of $CaMnO_{2.96}$ perovskite-type phase to $CaMnO_2$ rock-salt type, results to be highly topotactic and the oxidation process takes place at low temperature and rapid kinetic, leading to the perovskite starting material. This reversible process mainly implies oxygen diffusion through the structure, while the cationic subcell remains almost unalterable.

XRD and NPD data indicate $CaMnO_2$ to be a cubic single-phase rock-salt type suggesting a random distribution of Ca and Mn over the available metal cationic positions of the NaCl structure. However, the structural characterization performed at the local level clearly shows the presence of short ordered domains. Direct evidence of cationic order was obtained by SAED and dark field images were structural domains with a rhombohedral distortion of the cubic rock-salt unit cell ($a_R = \sqrt{2}a_{NaCl}$) are seen. Such a distortion is originated by a particular Ca/Mn arrangement at microscopic level giving rise to a

(31) Pask, J.E.; Singh, D.J.; Mazin, I.I.; Mellberg, C.S.; Kortus, J. *Phys. Rev. B* **2001**, *64*, 024403.
(32) Shull, C.G.; Strausser, W.A.; Wollan, E.O. *Phys Rev.* **1951**, *83*, 333.
(33) Roth, W.L. *Phys Rev.* **1958**, *110*, 1333.

nanodomains microstructure constituted by ordered nanoclusters into a NaCl-type matrix.

It is worth recalling that the same structural features are observed in $CaMnO_2$ prepared at high temperature. This fact strongly suggests that the cationic order is not determined by the topotactic reduction process but it is inherent to the $Ca_{0.5}Mn_{0.5}O_2$ structure. These results open the possibility of searching for new ordered pathways in the $Ca_{1-x}Mn_xO_2$ solid solution for those x values able to produce well known oxidized mixed oxides such as, for instance, Ca_2MnO_4 and $CaMn_2O_4$.

From a magnetic point of view, $CaMnO_2$ samples present antiferromagnetic interactions and show a typical behavior of diluted magnetic systems. $CaMnO_2$ and MnO present the same antiferromagnetic order; nevertheless, magnetostrictive distortion is not found in any of $CaMnO_2$ samples. The refined magnetic structure corresponds to a unit cell with twice the dimensions that the structural one.

Acknowledgment. Financial support through research Project No. MAT2004-01248 (Ministerio de Ciencia e Innovación (MCI), Spain) is acknowledged. S.d.D. thanks the MCI for financial support through a postgraduate grant.

JA901963M